journal

J. Am. Ceram. Soc., 95 [12] 3971–3978 (2012)
DOI: 10.1111/jace.12037

Computational Modeling of Grain Boundaries in ZrB_2: Implications for Lattice Thermal Conductivity

John W. Lawson,[‡,†] Murray S. Daw,[§] Thomas H. Squire,[¶] and Charles W. Bauschlicher Jr[‖]

[‡]Thermal Protection Materials Branch, NASA Ames Research Center, Mail Stop 234, Moffett Field 94035, California

[§]Department of Physics and Astronomy, Clemson University, Clemson 29631, South Carolina

[¶]Thermal Protection Materials Branch, NASA Ames Research Center, Mail Stop 234, Moffett Field 94035, California

[‖]Entry Systems and Technology Division, NASA Ames Research Center, Mail Stop 230-3, Moffett Field 94035, California

A combination of *ab initio*, atomistic, and finite element methods (FEM) was used to investigate fundamental properties of grain boundaries and grain boundary networks and their impact on lattice thermal conductivity in the ultra high-temperature ceramic ZrB_2. The structure, energetics, and lattice thermal conductance of certain low energy grain boundaries were studied. Atomic models of these boundaries were relaxed using density functional theory. Information about bonding across the interfaces was determined from the electron localization function. Interfacial thermal conductances were computed using nonequilibrium molecular dynamics. Microstructural models were used to determine the reduction in lattice thermal conductivity due grain boundary networks where FEM meshes were constructed on top of microstructural images.

I. Introduction

Ultra high-temperature ceramics (UHTC) are a class of materials with high melting points, good mechanical properties, and reasonable oxidation resistance. Among these materials, the metallic diborides, and especially ZrB_2, have been the object of considerable study, both as pure materials and as constituents in composites. These materials are of interest for applications in extreme environments which require little or no oxidation or ablation. In particular, they are candidate materials for sharp leading edges and nosecaps of hypersonic aircraft as well as propulsion systems, refractory crucibles, as well as other applications.[1] Unlike most ceramics, UHTCs are distinguished by their high thermal conductivity. High thermal conductivity offers a number of advantages for high-temperature applications. For example, high thermal conductivity can improve thermal shock resistance. It can also improve the efficiency of thermal radiation by rapidly redistributing thermal energy across available surfaces.

The total thermal conductivity κ_{tot} of the diborides has significant contributions from both electronic and lattice carriers.[2] The electronic component κ_e can be estimated approximately from knowledge of the electrical conductivity using the Weidemann-Franz (WF) empirical relation. The lattice contribution κ_{ph}, which results from phonon transport, cannot be measured directly and is usually inferred by subtracting κ_e from κ_{tot}. For single crystal ZrB_2, thermal conductivity measurements at room temperature have been reported as 140 W/(m·K) in the basal direction and 100 W/(m·K) along the *c*-axis.[3] These single sample results did not include either a characterization of the defect distribution, which will reduce κ_{tot}, or specific estimates of κ_e and κ_{ph}. Polycrystalline ZrB_2 has been more thoroughly studied. Previously, room temperature measurements have been reported as 55 W/(m·K) for ZrB_2 where κ_e was estimated to be 33 W/(m·K) and κ_{ph} was given as 22 W/(m·K).[2] More recent results[4] based on different processing methods quote values for κ_{tot} as high as 108 W/(m·K) for polycrystalline samples.

The reduction in κ_{tot} relative to single crystals comes primarily from the thermal resistance of grain boundaries. Variations in κ_{tot} with grain size can be substantial.[2,4] Whereas κ_e is expected to be relatively insensitive to grain boundaries due to the short electron mean free path, the lattice contribution κ_{ph}, which may be quite high in single crystals, can be reduced significantly due to grain boundary thermal resistance.[2] Different processing methods can lead to very different grain sizes and grain boundary structures. Therefore, it is important to understand the effect of grain boundaries on the properties of these materials.

In this study, we use a combination of *ab initio*, atomistic, and finite element methods (FEM) to study grain boundaries as well as grain boundary networks to understand their impact on lattice thermal conductivity in polycrystalline ZrB_2. Although we focus primarily on thermal conductivity, our results also have implications for mechanical response. Interatomic potentials for this material were derived previously.[5] These potentials have been used to compute the lattice thermal conductivity of single crystal ZrB_2.[6] In the present study, we first constructed a series of atomic models of grain boundaries for this material, namely coincidence and near coincidence *tilt* and *twist* boundaries. Both *ab initio* methods and the interatomic potentials were used to relax the structures and evaluate their energetics. The electron localization function (ELF) was used to provide spatially revolved information about bonding across the boundaries. This is especially useful for studying extended defects such as grain boundaries where the structures may undergo significant reconstruction. Understanding how the character of bonding changes across an interface can have important implications for properties. Next, the thermal resistance of the grain boundaries was computed using nonequilibrium molecular dynamics. It is important to note that single crystal lattice thermal conductivities as well as lattice thermal resistances of grain boundaries are not directly accessible to experimental measurement in these materials. However, these quantities can be determined directly from molecular dynamics (MD) simulations. Finally, microstructural calculations were performed to determine the reduction in the bulk lattice

W.-Y. Ching—contributing editor

Manuscript No. 31185. Received March 12, 2012; approved September 14, 2012.
[†]Author to whom correspondence should be addressed. e-mail: john.w.lawson@nasa.gov

thermal conductivity due to grain boundary networks. FEM computations were used to obtain the "effective thermal conductivity" of polycrystalline models where FEM meshes were constructed directly on SEM images.

II. Method

Ab initio computations were performed using density functional theory (DFT) and utilizing the functional of Perdew, Burke, and Ernzerhof.[7] Grain boundary structures were relaxed and their energetics evaluated. The plane wave code VASP and the projected augmented wave potentials were used for all calculations.[8,9] All results were converged with respect to k-point sampling and plane wave energy cut-off E_c. Periodic cells were used which resulted in two boundaries per cell.

The ELF can be evaluated during a DFT calculation. Specifically, the ELF gives the probability of finding an electron near a reference electron at a given point and with a fixed spin.[10] In this way, it is useful for identifying covalent bonds. The ELF is defined in terms of a dimensionless localization ratio $\chi_\sigma(r)$ which measures localization with respect to the uniform electron gas

$$\mathrm{ELF}(r) = \frac{1}{1+\chi_\sigma^2(r)} \tag{1}$$

The ELF takes values in the range $0 \leq \mathrm{ELF} \leq 1$ where ELF = 1 corresponds to perfect localization and ELF = 0.5 gives the electron gas. $\chi_\sigma(r)$ is computed directly from DFT quantities. The ELF can be contrasted against the electron charge density $\rho(r)$ which is a single electron quantity whereas the ELF gives information about the two-body distribution.

The nonequilibrium molecular dynamics method of Muller-Plathe (MP) was used to compute interfacial thermal conductances.[11,12] The LAMMPS package[13] together with the ZrB_2 interatomic potential "Pot 1" of Daw, Lawson, and Bauschlicher (DLB) were used for these computations. Periodic unit cells with a long direction ($\sim$100 nm) normal to the boundaries were created to minimize reflections. Convergence studies for both the normal and lateral dimensions were performed. Results were only weakly dependent on the lateral dimensions, however, which was typically ($\sim$1–5 nm). A NPT simulation was run at the given temperature for 100 ps to equilibrate the system. NVE simulations were then performed in which a "hot" region and a "cold" region were created on opposite sides of the boundaries by exchanging atoms between the two regions: the atom with the greatest kinetic energy in the cold region is swapped with the lowest kinetic energy atom in the hot region. A steady state was typically well established after 500 ps, resulting in a temperature gradient between the regions, and across the interfaces, where the heat flux Q was given by

$$Q = \frac{1}{2tA}\sum_i \frac{m}{2}\left(v_{i,\mathrm{hot}}^2 - v_{i,\mathrm{cold}}^2\right) \tag{2}$$

and where the sum is over the number of exchanges, t is the total simulation time, A is the cross-sectional area normal to the direction of heat flow, m is the atomic mass, and v_i is the velocity of the exchanged atom. At the interface, a discontinuity in the temperature profile (T versus z) will appear. The temperature discontinuity and the exchanged heat flux are related by the interfacial or Kapitza conductance σ_K

$$Q = \sigma_K \Delta T. \tag{3}$$

The inverse of the Kapitza conductance is the Kapitza resistance $R_K = 1/\sigma_K$. Steady-state temperature profiles were determined by averaging the temperature locally in narrow slices perpendicular to the boundaries and over runs of length 4 ns.

Finite element computations were performed using the open source code OOF2[14] and the commercial code MSCMarc. Finite element meshes were constructed directly on an SEM image of the microstructure of ZrB_2.[1] FEM meshes were created for both the grains and the boundaries, each of which was treated as a separate material with distinct thermal conductivities. Thus, the grain boundaries were treated as an "interphase." The effective thermal conductivity κ_{eff} of the full microstructure (grains + boundaries) was evaluated in three different ways. First, a transient thermal analysis was performed where a thermal flux was applied to one side of the system whereas the other sides were maintained as adiabatic boundaries. The temperature of the opposing side of the system (the "backface") was determined as a function of time. The κ_{eff} of the full polycrystal was evaluated by performing a second transient thermal analysis on an equivalent, homogeneous, reference material. The thermal conductivity of the reference was tuned to give a backface temperature trace that matched the polycrystalline result. Next, we performed a steady state thermal analysis using two different sets of boundary conditions. First, a uniform temperature gradient (UTG) was applied by fixing the temperature of opposite sides of the model. A transient thermal analysis was performed until the system reached steady state. Second, we applied a uniform heat flux (UHF) to opposite sides of the system until a steady state was reached. For both cases, UTG and UHF,

$$\langle q \rangle = -\kappa_{\mathrm{eff}} \cdot \langle \nabla T \rangle \tag{4}$$

where q is the heat flux, κ_{eff} is the effective thermal conductivity, ∇T is the temperature gradient, and the brackets represent volume averages over the system. Note for UTG, we fix ∇T and measure $\langle q \rangle$ after steady state is achieved. For UHF, we do the converse. Both methods were performed with boundary conditions applied in both the vertical and horizontal directions as well. It has been shown previously that $\kappa_{\mathrm{UHF}} < \kappa < \kappa_{\mathrm{UTG}}$.[15]

III. Structural Models

The crystal structure of single crystal ZrB_2, and the related material HfB_2, was discussed in detail in a previous publication.[16] To summarize, the structure of ZrB_2 is the AlB_2 type, designated as C32 with space group symmetry *P6/mmm*. This is a layered arrangement with alternating planes of pure Zr and pure B atoms. The Zr planes have a hexagonal close-packed structure whereas the B planes are open, hexagonal with six-membered rings resembling graphite. The layers are situated such that each Zr atom lies directly above and below the centers of six-membered B rings in the adjacent planes. The a and b-axis give symmetry equivalent in-plane directions whereas the c-axis is normal to the layers.

Structural models for ZrB_2 grain boundaries are considered for four situations: two twist boundaries and two tilt boundaries, one for each of the two independent axis, a and c. Hexagonal crystals with irrational ratios of their lattice parameters $(c/a)^2$ only have exact coincidence site lattice (CSL) boundaries corresponding to rotations about the c-axis.[17,18] We consider such CSL boundaries formed by twists and tilts about that axis. However, near coincidence boundaries about the a-axis can be formed by approximating $(c/a)^2$ as an rational number (m/n). This approximation will introduce a strain into the system. Smaller (n,m) values result in smaller, computationally efficient unit cells, but with larger strain. For larger values, the converse is true. For our structures, the strain was typically less than 1%. To accommodate *ab initio* computations, periodic cells were used, containing two boundaries per cell. With small cells, we expect nontrivial interaction between the boundaries. However we should

be able to obtain reliable information about relative structural and energetic differences.

For ceramics such as ZrB_2, grain boundaries are often disordered and may contain many impurities. However, such boundaries are usually the result of particular processing methods. Cleaner and more crystalline boundaries are expected to have low interfacial energies and therefore their formation should be favored with improved processing methods. Furthermore, such boundaries should have greater interfacial adhesion and reduced thermal resistance, and therefore are more desirable. Such boundaries are routinely observed in other ceramics such as alumina and zirconia.[19,20] In this study, we focus on these relatively simple boundaries both because of their computational efficiency and also because of their expected superior properties. We expect grain boundary thermal properties to be somewhat insensitive to the exact atomic structure of the boundary. Therefore, it is not necessary to find the absolute, lowest energy boundary structure, which can be a highly nontrivial task as has been shown in a recent work.[21]

The first boundary we consider is a $\Sigma 7$ symmetric tilt about the *c*-axis. This exact CSL boundary is shown in Fig. 1. As a shorthand we refer to this boundary as "*c*-tilt." For tilt boundaries, the tilt axis is parallel to the boundary plane. Because the Boron sublattice in ZrB_2 is graphitic, we propose a *c*-tilt grain boundary structure in analogy with graphite. Related structures have been recently proposed for graphene.[22] The boundary consists of a sequence of five and seven (5–7) membered Boron ring units that are separated by hexagonal rings. The distance between these units is related to the tilt angle where lower angles correspond to a larger separation between the five and seven pairs. The smallest such structure is the $\Sigma 7$ structure. To complete the structure for ZrB_2, Zr atoms are positioned over/above all Boron rings including the five- and seven-membered rings. This structure can also be viewed as an array of edge dislocations with a horizontal Burger's vector where the five-membered rings represent the extra plane of atoms.

The second boundary is a $\Sigma 7$ symmetric twist about the *c*-axis. We call this boundary "*c*-twist" and it is displayed in Fig. 2. For twist boundaries, the twist axis is perpendicular to the boundary plane. This boundary is the simplest of the ones we will consider and shows the least reconstruction. The interface structure has a layer of Zr and a layer of B shifted relative to each other. Thus, across the interface, the Zr atoms are not centered directly above and below Boron six-membered rings. This twist results in a small degree of crumpling of the two layers, mainly in the Boron layer. However, large-scale reconstruction does not occur because the intralayer interactions (metallic Zr and covalent B) have not been disturbed significantly. The interfacial layers also are further stabilized by the compounded effect of additional layers away from the boundary.

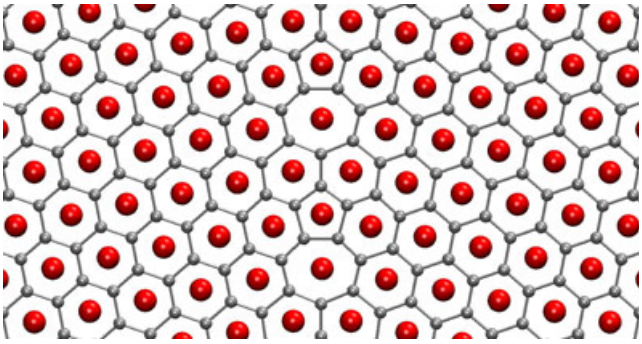

Fig. 1. Atomic structure of $\Sigma 7$ symmetric *c*-axis tilt boundary for ZrB_2 with Zr (red) and B (gray) atoms shown. The boundary contains 5–7 membered ring pairs separated by hexagonal rings. This structure is similar to ones proposed for graphene. The *c*-axis is normal to the plane of the figure and parallel to the boundary.

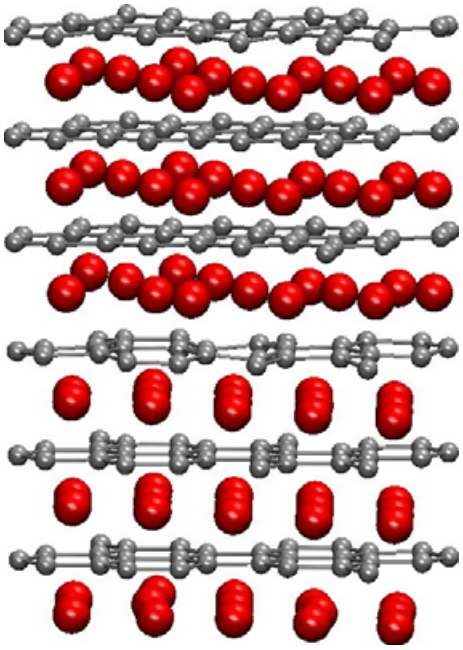

Fig. 2. Atomic structure of $\Sigma 7$ symmetric *c*-axis twist boundary for ZrB_2 with Zr (red) and B (gray) atoms shown. A layer of Zr has been shifted relative to a B layer resulting in crumpling. The *c*-axis is normal to the atomic layers and normal to the boundary.

The third structure we consider is a 90°, near-coincidence, asymmetric tilt boundary about the *a*-axis, which we call "*a*-tilt." This model contains two boundaries, which we designate Left and Right, as shown in Fig. 3. For the Left boundary, the inserted Zr layers match the middle section Boron layer. However, a deficit of Zr atoms now exists to match the Boron layer to the outer left. This results in an alternating series of flat and crumpled Boron rings in the Left interface. For the Right boundary, the Zr sheet matches perfectly the Boron layer to its right. However, there are too many Zr atoms in this layer to match the edge Boron layers on its left. These extra Zr atoms produce considerable crowding of the middle section Borons as can be seen in Fig. 8 from a different orientation where the Boron sheets are bent up or down at their edges.

The final boundary is a 90°, near coincidence, asymmetric twist about the *a*-axis, which we designate "*a*-twist." Figure 4 shows the periodic model for a-twist with two boundaries, denoted Left and Right. Both Left and Right boundaries have two sets of 90° rotated edge-on Boron planes interacting with each other. On the Left boundary, there is one Zr

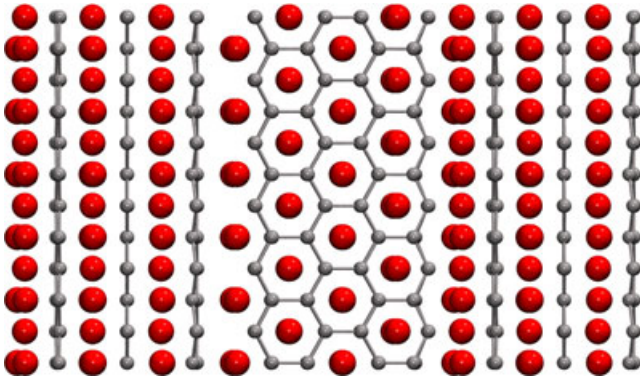

Fig. 3. Atomic structure of 90°, near coincidence, asymmetric *a*-axis tilt boundary for ZrB_2 with Zr (red) and B (gray) atoms shown. Unit cell has two boundaries designated Left and Right. A rotated view of this boundary can be seen in Fig. 7. The *a*-axis is in the plane of the figure and parallel to the boundary.

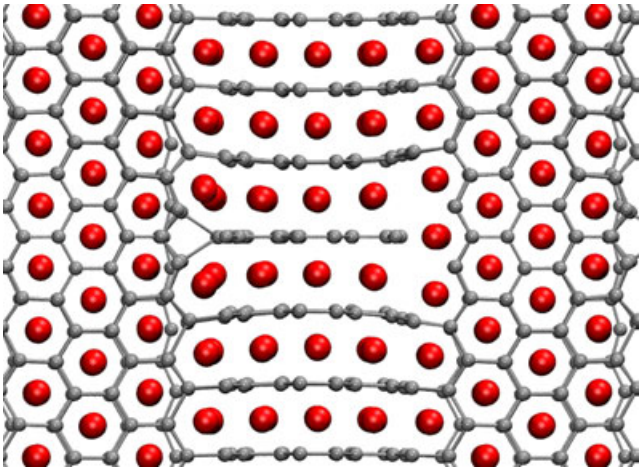

Fig. 4. Atomic structure of 90°, near coincidence, asymmetric *a*-axis twist boundary for ZrB_2 with Zr (red) and B (gray) atoms shown. Unit cell has two boundaries designated Left and Right. Significant reconstruction makes this the most disordered boundary. The *a*-axis is in the plane of the figure and normal to the boundaries.

atom too few per repeat unit, leaving an effective Zr vacancy in the center of the boundary. This results in a complicated four-membered Boron ring configuration. Above and below this ring, Zr atoms are pushed away, resulting in the bending of both Zr and B planes near that boundary. The Right interface has an extra Zr atom (actually a column of Zr going into the page of the figure) in this layer relative to the middle section. The extra Zr atom is effectively attached to the end of a Boron plane. Zr atoms above and below this atom are pushed away causing bending of the middle planes as they approach the boundary. We can see in the Boron plane that is edge-on to the extra Zr atom that the Boron rings are compressed along that edge.

Whereas *a*-twist and *a*-tilt have similar features, *a*-twist appears more disordered than *a*-tilt. This is a result of how the Boron planes interact with each other across their respective boundary. For *a*-tilt, the Boron planes on the left of the Left boundary and on the right of Right boundary are flat, chemically unreactive with no dangling bonds. The middle section of *a*-tilt has exposed edge-on Borons that could be reactive, but they are separated from the unreactive sheets by layers of large Zr atoms. For *a*-twist, the Boron sheets on both sides of both boundaries have the more reactive, edge-on configuration. This permits nontrivial Boron–Boron bonding across the interface and therefore a denser boundary. We will have more to say about this when we examine the electronic structure.

IV. Electronic Structure

The electronic structure of single crystal ZrB_2 was discussed in detail previously.[16] To summarize, the electronic configuration for Zr is $[Kr]5s^24d^2$, permitting two "s" and two "d" valence electrons to be donated to the material. Boron's electronic configuration is $[He]2s^22p^1$, giving it one less valence electron than Carbon. Thus, Boron has an electron "deficiency" which has a significant impact on its properties. Despite its simple atomic structure, ZrB_2 displays all three major electronic bonding motifs. The electron localization function (ELF) is a useful tool to identify and distinguish different types of bonding in the real space structure. In single crystal ZrB_2, the ELF in the metallic Zr layers is diffuse and relatively nonlocalized as expected for metallic bonding.[16] ELF accumulation points were identified in the Zr planes which aligned with Boron atomic sites in the neighboring planes. In the B planes, the electrons are well localized into covalent, highly directional bonds as reflected by high ELF values between neighboring Boron atoms. Between

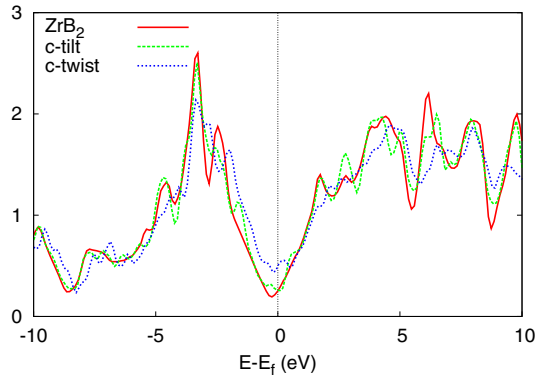

Fig. 5. Electronic densities of state for the *c*-axis tilt and *c*-axis twist boundaries compared to the single crystal result.

layers, significant charge transfer was found as electron "rich" Zr atoms donated electronic charge to the electron "deficient" Borons resulting in ionic bonding between layers. Thus, bonding in the Zr planes is metallic; bonding in the B planes is covalent; and the bonding between layers is ionic.

The electronic structure of grain boundaries can provide important information about interface properties.[18] The formation of an interface may result in significant reconstruction of the boundary atomic structure. The accompanying changes to the electronic structure can result in significant modifications to the bonding across the boundary. A range of scenarios is possible from the formation of localized states due to dangling bonds or impurity atoms to strong covalent bonding across the interface. In Fig. 5, we show the density of states (DOS) for the two simplest structures, *c*-tilt and *c*-twist, and compare them to the single crystal DOS. As can be seen, the electronic structures are largely similar for these cases and indicate that there are no localized states in these boundaries.

For grain boundaries, the ELF provides a spatially resolved description of how the bonding changes across the reconstructed interface; this can be correlated directly to interfacial properties such as adhesion, formation energies, and thermal conductance, among others. In Fig. 6, we show the ELF for *c*-tilt. *C*-tilt is one of the least disrupted boundaries. The material is still layered in the same way as with the single crystal, but at the boundary, 5–7 ring pairs are inserted which results in the different crystal orientation on either side of the boundary. The ELF clearly shows that the same bonding motifs survive the formation of this boundary, namely there is covalent bonding in the Boron planes including among the 5–7 rings. Regions of high ELF are seen between all Boron pairs regardless of the ring type (five-, six-, seven-membered rings). Interesting, the 5–7 rings remain flat without crumpling. Because of the strong covalent bonding across this interface, we expect especially strong interfacial adhesion and thermal conductance for this boundary.

The bonding structure for *c*-twist is relatively simple. The crystal structure on either side of the boundary remains intact except at the interface where a boron and a zirconium layer have been shifted relative to each other. We display the ELF for the boundary in Fig. 7. In particular, we consider the ELF in the plane on the Zr side of the boundary. This particular plane is sandwiched between two Boron planes. In the single crystal, the Boron planes are mirror images and the Zr ELF forms accumulation points in an open hexagonal lattice that are aligned precisely with the locations of the Borons in the two neighboring planes. In the case of *c*-twist, however, the Boron in the two neighboring planes is shifted relative to each other. Therefore, the ELF accumulation points in the Zr plane are no longer aligned with the Boron atoms across the interface. The implication of this is not completely clear, but it is expected that this mismatch will weaken the ionic bonding across the interface.

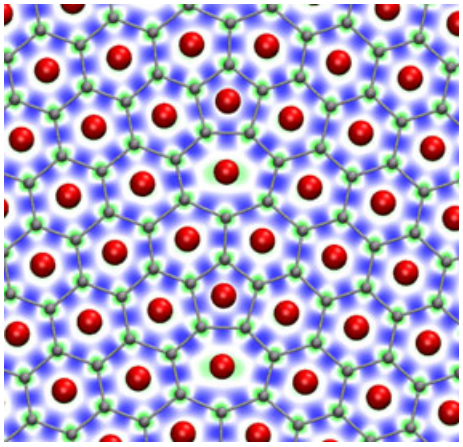

Fig. 6. ELF for the *c*-tilt boundary showing a cut through a Boron plane. Blue is high ELF and green is low ELF. High ELF exists between all Boron pairs regardless of the ring type (5-,6-,7-membered rings). Good interfacial adhesion and thermal conductance are expected due to strong covalent bonding across the boundary.

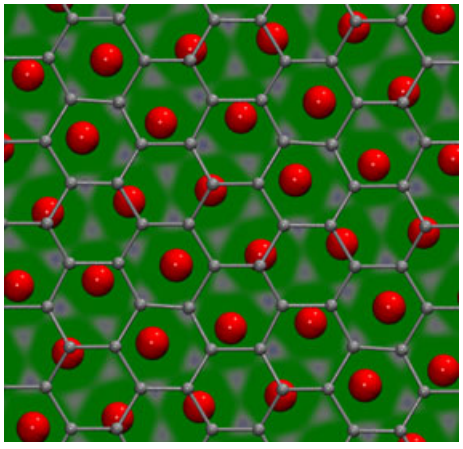

Fig. 7. ELF for the *c*-twist boundary where a Boron and a Zirconium layer have been shifted relative to each other. The figure shows a cut through a metallic Zr plane. Blue is high ELF and green is low ELF. The single crystal ELF has accumulation points in the Zr plane that are aligned with Borons atoms in the neighboring planes. For *c*-twist, the accumulation points in the Zr plane have been shifted which is expected to weaken the boundary.

In Fig. 8, the ELF for *a*-tilt is shown in a plane crossing the boundary where the orientation has been rotated with respect to Fig. 3. The ELF plane displayed in Fig. 8 contains only Boron atoms on both sides of the interfaces. The Zr atoms in the figure are in front of the contour plane. The plane that is displayed has the maximum ELF at the interface. The bonding across the Left boundary is expected to be ionic due to the Zr–B interaction. However, we see evidence from the ELF plot of some nontrivial electron localization inside the interface involving pairs of B atoms. These Boron ELF clouds are distorted slightly and may enhance the interaction across the interface. On the Right boundary, we have bending of Boron planes. The ELF plot shows that pockets of localized electrons are also seen associated with B pairs atoms across the boundary. In this case, some of the B pairs have been distorted relative to their position on the Left boundary. The Right boundary is more complex than the Left boundary as there are Zr–Zr interactions in addition to Zr–B and B–B interactions.

In Fig. 9, we show an ELF contour plot for *a*-twist; the plane displayed has the maximum ELF across the interfaces. Due to the reactive edge-on Boron plane interacting at both interfaces, a-twist has complex bonding across its boundaries.

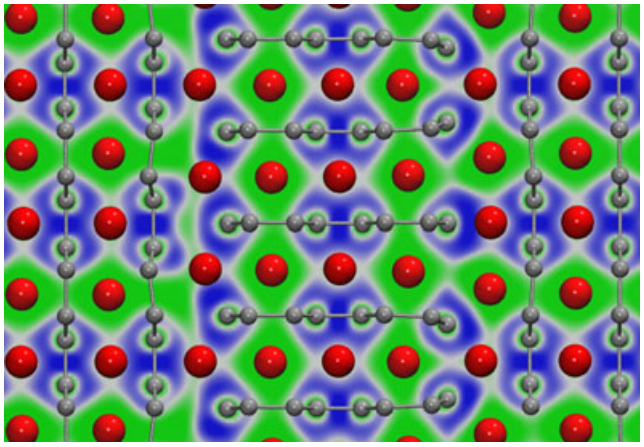

Fig. 8. ELF for the asymmetric *a*-tilt boundary. The figure shows a cut plane with only Boron atoms and with the maximum ELF in the boundary. Blue is high ELF and green is low ELF. Bonding across the Left boundary is expected to be ionic due to the Zr–B interaction. The ELF plot shows localization inside the interface involving pairs of B atoms. These Boron ELF clouds may enhance the interaction across the interface. On the Right boundary, Boron planes are bent due to crowding from extra Zr atoms.

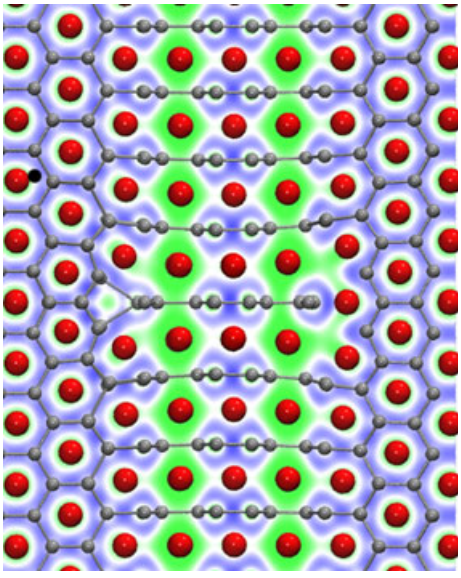

Fig. 9. ELF for the asymmetric *a*-twist boundary. Blue is high ELF and green is low ELF. The figure is in a cut plane that contains only Borons and has the maximum ELF in the boundary. Reactive edge-on Boron planes at both interfaces create complex bonding across its boundaries. The horizontal Boron plane in the center of the figure intersects the two boundaries differently. At the Left boundary, four-membered covalent Boron rings form. At the Right boundary, the Boron plane is compressed due to an extra Zr atom in the interface. Strong covalent bonding is seen across both Left and Right boundaries.

A central exotic feature of this structure is the horizontal Boron plane in the center of the middle section of Fig. 9. This Boron plane intersects the two boundaries in very different ways. At the Left boundary where there are missing Zr atoms, four-membered covalent Boron rings form. The ELF shows that there is strong covalent bonding in this ring that reaches across the Left interface. At the Right boundary, the same Boron plane encounters an extra Zr atom at that interface. As a result, this particular Boron plane is compressed relative to the other Boron planes. There is strong covalent bonding across both Left and Right interfaces, resulting from six-membered rings twisted at 90° relative to each other across the interfaces, but still covalently bonded to each other. In addition, most of the Zr atoms in both boundaries are surrounded

by Boron structures on five sides, instead of the single crystal configuration with Borons only above and below the Zr. Thus, there is nontrivial and complex electronic structure between these Zr and their Boron-rich caged structures.

V. Grain Boundary Energetics

The grain boundary interfacial excess energy was defined as

$$\gamma = (E_{GB} - nE_{bulk})/2A \quad (5)$$

where E_{GB} is the total energy of the grain boundary cell, E_{bulk} is the total energy of a formula unit of single crystal bulk material, n is the number of formula units to match the number of atoms in the grain boundary cell, and A is the area of the interface. The volume of the interface was defined as

$$\Delta_z = (z_{GB} - z_{bulk})/2 \quad (6)$$

where z_{GB} is the length of the relaxed cell in the direction normal to the boundary and z_{bulk} is the length of an equivalent cell with no boundary.

These quantities were calculated for unit cells corresponding to the structures shown in Figs. 1–4 using *ab initio* computations and also using the ZrB_2 DLB interatomic potentials. The results are shown in Table I. With such small cells (from 72 atoms for *a*-tilt to 1344 atoms for *a*-twist), significant interactions are expected between the two boundaries in each cell. As previously discussed, *c*-tilt and *c*-twist are exact CSL boundaries whereas *a*-tilt and *a*-twist are near-CSL structures. The near-CSL interfaces have a small amount of artificial strain (less than 1%). To maintain these structures, their volume was fixed during the optimization and only the ionic positions were allowed to relax. Because of the fixed volume, Δ_z will necessarily be zero for these cases. Both of these factors, interface interactions and unit cell strain, will affect our results in absolute terms, however, relative differences can be considered. In addition, comparison with *ab initio* results will help access the accuracy of the DLB potentials.

In Table I, the relaxed and unrelaxed (in parenthesis) interfacial energies are given. The amount of relaxation in the energy is related to the degree of reconstruction of the structures. *C*-tilt and *c*-twist have the lowest interfacial energies with 153 and 157 meV/Å^2, respectively, compared to 227 meV/Å^2 for a-tilt and 212 meV/Å^2 for *a*-twist. *A*-tilt and *a*-twist have considerably more reconstruction compared with *c*-tilt and *c*-twist as indicated by the significant energetic relaxation in these structures. It is somewhat surprising that *a*-tilt has a higher energy than *a*-twist as *a*-twist is more disordered. However, the significant covalent bonding across the *a*-twist interfaces may be a factor in reducing its energy relative to *a*-tilt. The results for *c*-tilt and *c*-twist are consistent with the intuition that they are the least reconstructed structures and therefore should be the easiest to form. They are also low Σ CSL boundaries and therefore are expected to have low energies. An *ab initio* number for Δ_z can only be evaluated for *c*-twist and that value is 0.29 Å.

Table I. Energetics and Thermal Conductance for ZrB_2 Grain Boundary Structures from Empirical Potentials (DLB/Pot 1) and *ab initio*/DFT. Unrelaxed quantities are in parenthesis

	Ab initio		DLB/Pot 1		
	γ (meV/Å^2)	Δ_z (Å)	γ (meV/Å^2)	Δ_z (Å)	σ_K ($GW/(m^2 \cdot K)$)
c-tilt	153 (369)	–	112 (238)	–	1.77
c-twist	157 (375)	0.29	111 (258)	0.29	0.58
a-tilt	227 (1040)	–	107 (1380)	–	0.38/0.31
a-twist	212 (1230)	–	118 (1430)	–	0.55/0.53

Interfacial energies from the interatomic potential are very similar among the boundaries, with a variation of a few percent. Results are consistently lower for the potentials compared with the *ab initio* numbers, in the case of *a*-tilt and *a*-twist by a factor of 2X. The highest energy from the potentials is 118 meV/Å^2 for *a*-twist and the lowest is 107 meV/Å^2 for *a*-tilt. Given the similarity of these numbers, it is difficult to establish a clear ordering. However, the degree of relaxation is consistent with the *ab initio* results with a much smaller amount of relaxation for *c*-tilt and *c*-twist compared with *a*-tilt and *a*-twist. The results for Δ_z for *c*-twist agree very well with the *ab initio* number. It is clear, however, that the DLB potential does better for unrelaxed energies than relaxed. In fact, the expected ordering of the relaxed boundaries, as suggested by the *ab initio* results, is not well reproduced by DLB.

VI. Thermal Resistance

In Table I, we also present values for the thermal conductance of each boundary. These calculations were all performed at 300 K. Thermal profiles for the four boundaries are shown in Fig. 10. Unit cells were typically more than 200 nm in length to minimize reflections. The longest cell had a length of 248 nm for *c*-twist. *A*-twist which had an unusually large lateral cross-section was the smallest at 109 nm in length. Note that *c*-tilt and *c*-twist are symmetric boundaries whereas *a*-tilt and *a*-twist are asymmetric. Therefore, if the two boundaries in a unit cell are symmetric, they will both have same σ_K. In the asymmetric case, they can be different as indicated in the Table.

Some degree of correlation is expected between the interfacial energy γ and the thermal conductance σ_K. In particular, boundaries with low γ should have high σ_K. The variation among the σ_K values, however, is much greater than the variation among γ values from the potentials. Thus, establishing a clear relation is not obvious. However, the σ_K values do correspond to our intuition for these structures. *C*-tilt has the highest conductance with 1.77 GW/(K·m^2). The fact that *c*-tilt should have a high thermal conductance is not surprising as the structural disruption of that boundary is relatively small and the strong covalent bonding across the boundaries should permit a smooth flow of thermal energy. It is interesting, however, that *c*-tilt which has a γ values on par with *c*-twist at the *ab initio* level has a much larger value for the thermal conductance σ_K. This may be due to the fact that thermal conductivity values are higher in-plane compared with normal directions. Therefore, in-plane interfacial conductances may be expected to be higher than for normal interfaces. *A*-twist and *c*-twist have very similar conductances with 0.55/0.53 GW/(K·m^2) and 0.58 GW/(K·m^2). Their γ values from the potentials are very similar; however, a much larger gap is seen in their *ab initio* γ values. *A*-tilt has the lowest conductances with values of 0.38/0.31 GW/(K·m^2) for the Left and Right boundaries. The *a*-tilt γ value is similar to *a*-twist at the *ab initio* level. However, we expect *a*-twist to have a higher thermal conductance than *a*-tilt because of the significant covalent bonding across that interface.

VII. Microstructural Modeling

The effect of grain boundary networks on the lattice thermal conductivity of polycrystal ZrB_2 is now considered. To begin, a Brick Layer Model (BLM) was used to estimate the reduction in thermal conductivity due to interfacial thermal resistance.[23] In the BLM, the effective thermal conductivity κ_{eff} is given by

$$\frac{1}{\kappa_{eff}} = \frac{1}{\kappa_0} + \frac{R_K}{d} \quad (7)$$

where κ_0 is the intrinsic lattice thermal conductivity of the material, R_K is the interfacial (Kapitza) thermal resistance,

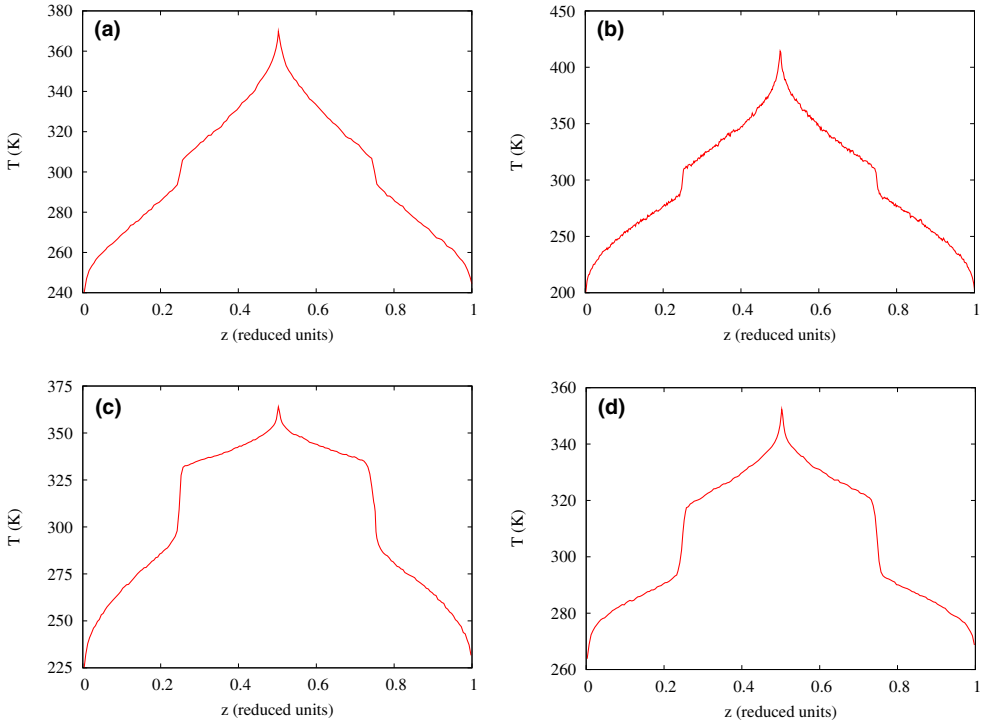

Fig. 10. Temperature profiles versus simulation cell distance normal to the grain boundaries for *c*-tilt (a), *c*-twist (b), *a*-tilt (c), and *a*-twist (d). Cell distance is in reduced units. Grain boundaries are positioned at $z = 0.25$ and $z = 0.75$. Heat source is at $z = 0.5$ and heat sink is at $z = 0/1$.

and d is the grain size. This expression states that the effective resistance is a sum of the intrinsic resistance plus the sum of the resistances for each boundary crossed. The effective thermal conductivity κ_{eff} was evaluated using thermal parameters taken from our atomistic simulations. The value of κ_0 cannot be measured directly therefore we assigned a value of 50 W/(m·K) which was obtained from our previous atomistic computations.[6] This value is the average of the in-plane and normal conductivities obtained from those simulations. For R_K, we used the value for *a*-tilt which has the highest interfacial resistance of our structures, 3.3 (m^2·K)/GW. For d we used 6μm which is typical for these materials. The effective thermal conductivity κ_{eff} obtained was 48.6 W/(m·K) which represents a very small reduction in its thermal conductivity from the intrinsic value κ_0. Experimental thermal conductivity values reported by Zimmerman *et al.*[2] are around 22 W/(m·K) at room temperature. This suggests that the boundaries considered in this study have very low interfacial thermal resistance from the MD simulations compared with experimental data. This is not surprising as our structures are very pristine and current processing methods for this material typically give much more disordered boundaries with numerous impurities. On the other hand, this also shows that significant improvement in material properties can be obtained by improving the quality of the grain boundaries.

Next, we considered an experimentally more representative situation. First, we utilized a more realistic microstructure than BLM(1D boundaries "in series"). In particular, we evaluated κ_{eff} using FEM computations whose mesh was constructed on an SEM micrograph taken from Ref. 1. Second, FEM thermal parameters were taken from experiment to obtain a nontrivial reduction in κ_{eff}. For the thermal conductivity of the grains, we again assigned a value 50 W/(m·K) obtained from MD simulations. However, as the MD interfacial resistances were very low (significantly lower than what is expected for these materials), a more realistic value for σ_K was chosen to be 10.0 MW/(m^2·K).[24] An interphase conductivity κ_K was obtained by multiplying σ_K by a representative width, giving $\kappa_K = 1\ W/(m{\cdot}K)$. In Fig. 11, we show the original SEM image, the FEM mesh, and the steady-state temperature distribution in the material. As we can see, the conduction is not uniform as the grain boundary network impedes the flow, resulting in jagged thermal contours through the material. Remarkably, the result for the effective thermal conductivity of the material from the transient analysis is 18 W/(m·K) which is very close to the experimental value of 22 W/(m·K). In addition, results from the UTG and UHF steady-state computations are reported in Table II. Those numbers agree very well with each other and with the transient result.

It is interesting to compare the FEM result with the BLM and also with the rule of mixtures using the same parameters. Using the BLM expression and the more realistic interfacial

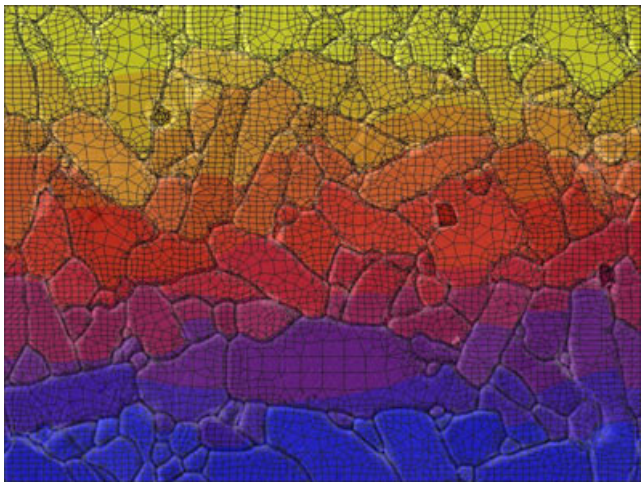

Fig. 11. Steady-state FEM thermal analysis for a ZrB_2 microstructure. FEM mesh was constructed on top of an SEM image.[1] Figure shows the original image, the FEM mesh, and constant temperature contours thermal solution. Yellow is high temperature and blue is low temperature.

Table II. Effective Thermal Conductivity Values ($W/(m \cdot K)$) for the SEM Microstructure from FEM Computations, the Brick Layer Model (BLM), the Rule of Mixtures (ROM), and the Experimental Value.[2] FEM Computations are Obtained from a Transient Method as well as Two Steady-State Approaches using the Uniform Temperature Gradient UTG Boundary Condition and the Uniform Heat Flux UHF Boundary Condition. Vertical and Horizontal (with Respect to the Image) Directions of Heat Transport were Considered. The Last Column Gives the Average if the Result is Direction Dependent

κ_{eff}	Vertical	Horizontal	
FEM/Transient	18		18
FEM/UTG	17.5	16.2	16.8
FEM/UHF	16.7	15.9	16.3
BLM			10
ROM			44
Exp.			22

parameters, we obtain 10.1 W/(m·K) for κ_{eff}. This is a reasonable result as the BLM is a series resistance model and therefore should be lower than the FEM model which has both series and parallel contributions. As the FEM model is a two-phase system we can also apply the rule of mixtures which gives for this situation 44 W/(m·K). The rule of mixtures describes a system of parallel resistances, therefore, it should give an upper bound relative to the FEM model. These calculations show that a wide variation of results can be obtained depending on which model microstructure is used.

VIII. Conclusion

In this study, we used a combination of *ab initio* computations, atomistic simulations, and FEM calculations to study the structure and properties of grain boundaries and grain boundary networks and investigate their impact on lattice thermal conductivity in ZrB_2. *Ab initio* results showed that the *c*-axis CSL boundaries, *c*-tilt and *c*-twist, had lower interfacial energies than the *a*-axis near-CSL boundaries, *a*-tilt and *a*-twist. Energetics from the interatomic potential did not produce as clear an ordering, giving interfacial energies very similar to each other. However, the absolute values of the energies from the potentials were reasonable. The degree of energetic relaxation of the structures matched very well the *ab initio* results. In general, the new interatomic potential developed for this material seemed to give a reasonable description of the boundaries.

Interfacial thermal conductances σ_K were evaluated using nonequilibrium molecular dynamics. For our boundaries, *c*-tilt had the lowest thermal resistance. The highest interfacial thermal resistances were for *a*-tilt which was both more disordered and more ionic than the other boundaries. In general, however, all four boundaries had very low thermal resistances compared with estimates based on experimental data. That is not surprising as these boundaries are very crystalline, highly ordered, and free of impurities. These calculations show, however, that low energy structures with very favorable properties exist for these materials and might be produced by improved processing methods.

The effect of the grain boundary network on the bulk lattice thermal conductivity of the material was also considered. A FEM thermal analysis was performed using a microstructure obtained from an SEM image. The FEM computations showed a reduction in lattice thermal conductivity that was much closer to experiments than results obtained from simple analytic models such as the BLM or the ROM.

Acknowledgments

M.S.D. was supported under a NASA prime contract to ELORET Corporation. We benefited from discussions with Pawel Keblinski and Tapan Desai.

References

[1]W. G. Fahrenholtz, G. E. Hilmas, I. G. Talmy, and J. A. Zaykoski, "Refractory Diborides of Zirconium and Hafnium," *J. Am. Ceram. Soc.*, **90**, 1347–64 (2007).

[2]J. W. Zimmermann, G. E. Hilmas, W. G. Fahrenholtz, R. B. Dinwiddie, W. D. Porter, and H. Wang, "Thermophysical Properties of ZrB_2 and ZrB_2SiC Ceramics," *J. Am. Cerm. Soc.*, **91**, 1405–11 (2008).

[3]H. Kinoshita, S. Otani, S. Kamiyama, H. Amano, I. Akasaki, J. Suda, and H. Matsunami, "Zirconium Diboride (0001) as an Electrically Conductive Lattice-Matched Substrate for Gallium Nitride," *Jpn. J. Appl. Phys.*, **40**, L1280–82 (2001).

[4]L. Zhang, D. A. Pejakovic, J. Marschall, and M. Gasch, "Thermal and Electrical Transport Properties of Spark Plasma-Sintered HfB_2 and ZrB_2 Ceramics," *J. Am. Cerm. Soc.*, **94**, 2562–70 (2011).

[5]M. S. Daw, J. W. Lawson, and C. W. Bauschlicher, "Interatomic Potentials for Zirconium Diboride and Hafnium Diboride," *Comp. Mat. Sci.*, **50**, 2828–35 (2011).

[6]J. W. Lawson, M. S. Daw, and C. W. Bauschlicher, "Lattice Thermal Conductivity ZrB_2 and HfB_2 from Atomistic Simulations," *J. Appl. Phys.*, **11**, 083507–11 (2011).

[7]J. Perdew, K. Burke, and M. Ernzerhof, "Generalized Gradient Approximation Made Simple," *Phys. Rev. Lett.*, **77** 3865–69 (1996).

[8]G. Kresse and J. Furthmüller, "Efficient Iterative Schemes for Ab Initio Total-Energy Calculations Using a Plane-Wave Basis Set," *Phys. Rev. B*, **54** 11169–86 (1996).

[9]G. Kresse and D. Joubert, "From Ultrasoft Pseudopotentials to the Projector Augmented-Wave Method," *Phys. Rev. B*, **59**, 1758–75 (1999).

[10]A. D. Becke and K. E. Edgecombe, "A Simple Measure of Electron Localization in Atomic and Molecular Systems," *J. Chem. Phys.*, **92**, 5397–403 (1990).

[11]F. Muller-Plathe, "A Simple Nonequilibrium Molecular Dynamics Method for Calculating the Thermal Conductivity," *J. Chem. Phys.*, **106**, 6082–86 (1997).

[12]P. K. Schelling, S. R. Phillpot, and P. Keblinski, "Kapitza Conductance and Phonon Scattering at Grain Boundaries by Simulations," *J. Appl. Phys.*, **95**, 6082–92 (2004).

[13]S. Plimpton, "Fast Parallel Algorithms for Short-Range Molecular Dynamics," *J. Comp. Phys.*, **117**, 1–19 (1995).

[14]A. C. E. Reid, S. A. Langer, R. C. Lua, V. R. Coffman, S. I. Haan, and R. E. García, "Image-Based Finite Element Mesh Construction for Material Microstructures," *Comp. Mat. Sci.*, **43**, 989–99 (2008).

[15]S. Hazanov and C. Huet, "Order Relationships for Boundary Conditions Effect in Heterogeneous Bodies Smaller Than the Representative Volume," *J. Mech. Phys. Solids*, **42**, 1995–201 (1994).

[16]J. W. Lawson, C. W. Bauschlicher, and M. S. Daw, "Ab Initio Calculations of Electronic, Mechanical and Thermal Properties of ZrB_2 and HfB_2," *J. Am. Ceram. Soc.*, **94**, 3494–9 (2011).

[17]D. H. Warrington, "The Coincidence Site Lattice (CSL) and Grain Boundary (DSC) Dislocations for the Hexagonal Lattice," *J. de Physique*, **36**, C4-87–C4-95 (1975).

[18]A. P. Sutton and R. W. Balluffi, *Interfaces in Crystalline Materials*. Clarendon, New York, 1995.

[19]E. C. Dickey, X. Fan, and S. J Pennycook, "Structure and Chemistry of Yttria-Stabilized Cubic-Zirconia Symmetric Tilt Grain Boundaries," *J. Am. Ceram. Soc.*, **84**, 1361–8 (2001).

[20]J. P. Buban, K. Matsunaga, J. Chen, N. Shibata, W. Y. Ching, T. Yamamoto, and Y. Ikuhara, "Grain Boundary Strengthening in Alumina by Rare Earth Impurities," *Science*, **311**, 212–5 (2006).

[21]A. L.-S. Chua, N. A. Benedek, L. Chen, M. W. Finnis, and A. P. Sutton, "A Genetic Algorithm for Predicting the Structures of Interfaces in Multicomponent Systems," *Nat. Mat.*, **9**, 418–22 (2010).

[22]R. Grantab, V. B. Shenoy, and R. S. Ruoff, "Anomalous Strength Characteristics of Tilt Grain Boundaries in Graphene," *Science*, **330**, 946–8 (2010).

[23]D. S. Smith, S. Fayette, S. Grandjean, C. Martin, R. Telle, and T. Tonnessen, "Thermal Resistance of Grain Boundaries in Alumina Ceramics and Refractories," *J. Am. Ceram. Soc.*, **86**, 105–11 (2003).

[24]D. G. Cahill, W. K. Ford, K. E. Goodson, G. D. Mahan, A. Majumbar, H. J. Maris, R. Merlin, and S. R. Philpot, "Nanoscale Thermal Transport," *J. Appl. Phys.*, **93**, 793–818 (2003). □